

Secondary Electron Emission by Plasmon-Induced Symmetry Breaking in Highly Oriented Pyrolytic Graphite

Wolfgang S. M. Werner¹,* Vytautas Astašauskas², and Philipp Ziegler¹

Institut für Angewandte Physik, Technische Universität Wien, Wiedner Hauptstraße 8-10/134, A-1040 Vienna, Austria

Alessandra Bellissimo³† and Giovanni Stefani³‡

Dipartimento di Scienze, Università degli Studi Roma Tre, Via della Vasca Navale 84, I-00146 Rome, Italy

Lukas Linhart¹ and Florian Libisch¹

Institut für Theoretische Physik, Technische Universität Wien, Wiedner Hauptstraße 8-10/136, A-1040 Vienna, Austria



(Received 9 June 2020; accepted 15 September 2020; published 6 November 2020)

Two-particle spectroscopy with correlated electron pairs is used to establish the causal link between the secondary electron spectrum, the $(\pi + \sigma)$ plasmon peak, and the unoccupied band structure of highly oriented pyrolytic graphite. The plasmon spectrum is resolved with respect to the involved interband transitions and clearly exhibits final state effects, in particular due to the energy gap between the interlayer resonances along the ΓA direction. The corresponding final state effects can also be identified in the secondary electron spectrum. Interpretation of the results is performed on the basis of density-functional theory and tight-binding calculations. Excitation of the plasmon perturbs the symmetry of the system and leads to hybridization of the interlayer resonances with atomlike σ^* bands along the ΓA direction. These hybrid states have a high density of states as well as sufficient mobility along the graphite c axis leading to the sharp ~ 3 eV resonance in the spectrum of emitted secondary electrons reported throughout the literature.

DOI: [10.1103/PhysRevLett.125.196603](https://doi.org/10.1103/PhysRevLett.125.196603)

Van der Waals materials have recently been attracting interest in materials science since they exhibit outstanding fundamental and technological properties and are building blocks for multilayered quasi-2D materials, as well as 3D materials and heterostructures [1,2]. Graphite, being a model system for this class of materials has been most extensively studied with respect to its electronic structure, both experimentally [3–13] and theoretically [14–19].

When two or more graphene layers are put on top of each other, so-called interlayer resonances form in the electronic structure, which are highly dispersive along the c axis and reflect the three-dimensional structure of the crystal [20]. Distinct oscillations in the electron reflectivity are observed when measuring the reflected intensity as a function of the electron kinetic energy [21–23], their number being equal to the number of graphene layers minus one. Interlayer states are highly transmissive for electrons coming from vacuum and have a large local density of states in between individual graphene layers. For graphite they appear as a broad band of states that strongly couple to vacuum [24]. The character of such electronic multiquantum well states can be qualitatively understood using the analogy to a Fabry-Pérot interferometer in light optics [25]. The signal employed in the above techniques, such as elastic peak electron spectroscopy [25] and total current spectroscopy [11], exclusively stems from impinging electrons, which

are eventually detected without having suffered any energy loss or are absorbed in their entirety, such as in inverse photoemission spectroscopy (IPES) experiments [20].

Compared to the works cited above, the present Letter concerns the reverse process, where electrons are leaving the surface after being liberated inside the solid. This phenomenon of secondary electron emission (SEE) is of great fundamental as well as technological importance [24]. In the past, SEE has also extensively been employed to study the unoccupied electronic structure of graphite [4–7,9,10,26]. Obviously, for secondary electron emission, energy losses, in particular, excitation and decay of plasmons [27–33], play an essential role. A striking difference between electronic structure data from SEE and the *elastic* techniques mentioned in the previous paragraph is that the dispersion of the interlayer resonances is not at all observed in SEE data. Instead, a strong resonance is found in secondary electron spectra, which always appears at an energy of about 3 eV above vacuum (i.e., within the energy range of the first interlayer state above vacuum). The position of this resonance shows no dispersion whatsoever in SEE data and is found to be independent of the experimental kinematics in a substantial number of works by different authors [3–7,9–11].

We use time-correlated two-electron spectroscopy to establish a causal relationship between energy losses and

secondary electron emission [34–38] on a sample of highly oriented pyrolytic graphite (HOPG). In particular, secondary electron-electron energy loss coincidence spectroscopy is employed (see Supplemental Material [39]) to investigate the relationship between energy losses suffered by exciting a plasmon and the concomitant emission of a secondary electron. Note that, for a given energy loss of the primary electron to be feasible, corresponding initial and final states need to exist for the liberated electron in order to satisfy energy and momentum conservation. The electronic transitions taking place in resonance with the plasmon are explicitly identified experimentally. The experimental results highlight the influence of the complex band structure of HOPG on the plasmon spectrum and the ejection of a secondary electron in the course of the associated interband transition and are interpreted with the aid of density functional theory (DFT) and tight-binding calculations [39]. In particular, when the symmetry of the system is broken in our tight-binding model, the resulting hybridization of the interlayer states with the atomlike σ_2^* band leads to the ~ 3 eV resonance in the secondary electron (SE) spectrum.

Our experimental results are summarized in Figs. 1–3(a) showing different portions of the electron coincidence spectrum taken in specular reflection geometry at the Bragg maximum for a primary energy of $E_0 - E_{\text{vac}} = 173$ eV (see Ref. [39] for details). The white curve in Figs. 1 and 2(a) represents the singles electron spectrum, exhibiting the elastic peak as well as the π and $(\pi + \sigma)$

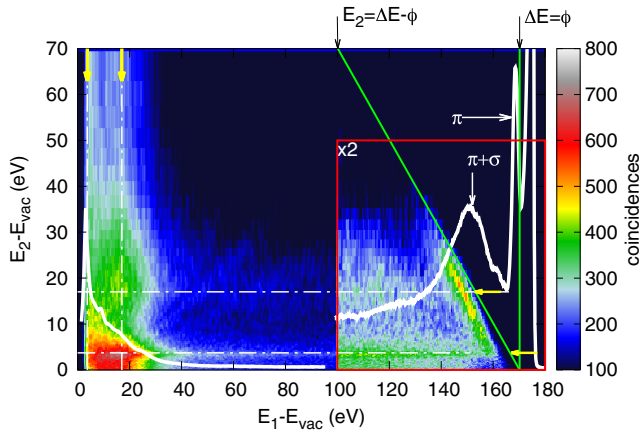


FIG. 1. Double differential spectrum of true coincidences for HOPG for an incident energy of 173 eV above vacuum (energy resolution $\delta E_1 = 5$ eV). The white curve is the singles loss and secondary electron spectrum. Indices 1 and 2 are used to indicate, respectively, fast and slow electrons arriving at detector 1, the hemispherical mirror analyzer, and 2, the time of flight (TOF) analyzer [39]. The green line labeled $E_2 = \Delta E - \phi$ indicates the minimum energy loss needed for the slow liberated electron (2) to reach the vacuum level from the Fermi level for a given energy loss ΔE , where $\phi = 4.6$ eV is the work function of HOPG. Here and below, the yellow arrows correspond to final state energies of $E_f - E_{\text{vac}} = 3.7$ and 17 eV, respectively.

plasmon losses, defined by the energies for which the real part of the dielectric function crosses zero, at $\hbar\omega_\pi \sim 6$ and $\hbar\omega_{\pi+\sigma} \sim 23$ eV [3]. For higher energy losses, plural plasmon excitation sets in. The secondary electron spectrum is characterized by a very sharp peak at 3.7 eV, which has been reported earlier by many authors [4,6,7,9–11,24,26,40–42], and a broad shoulder at ~ 17 eV.

The coincidence spectrum shown in false colors in Fig. 1 represents the number of correlated electron pairs emitted with a given combination of energies (E_1, E_2) . When recording the spectrum of correlated electrons in a Bragg maximum, those processes dominate in which the primary electron is first deflected along the outgoing Bragg beam, followed by the inelastic process. In the deflection-loss (DL) model, one thus assumes the initial momentum of the primary electron to be exactly defined by the Bragg condition [8,44–46] before the loss process liberating the second electron of the pair takes place. As a consequence,

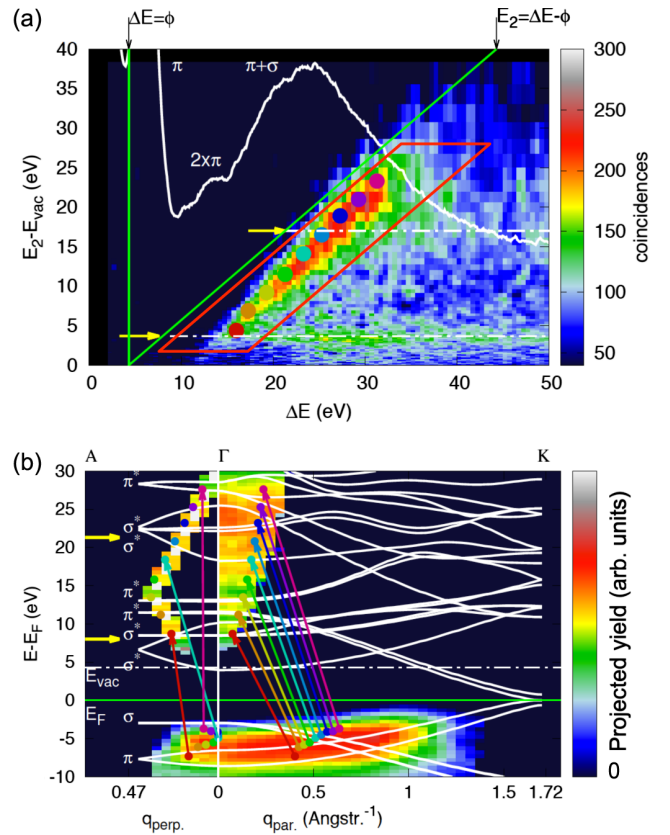


FIG. 2. (a) Coincidence spectrum of the plasmon loss in HOPG (measured with an energy resolution $\delta E_1 = 1.25$ eV.) The white curve is the singles loss spectrum. (b) The data in the plasmon feature in (a) within the red parallelogram represented in k space and projected on the pertinent band structure [43] along the ΓA and ΓK direction (see Supplemental Material [39]). The colored arrows indicate transitions associated with the dots in the coincidence yield in (a). Their colors correspond to those of the dots in (a), while the false colors in (a) and (b) represent intensities, as indicated by the color bars.

all initial and final states of the inelastic process are fixed by momentum and energy conservation [39,45]. In other words, the coincidence experiment makes it possible to pinpoint the electronic transition of the bound electron involved in the $(e, 2e)$ process by measuring time-correlated electron pair intensities. In the present case, this mainly concerns emission of a secondary electron after excitation and decay of a plasmon by the primary electron.

Three distinctly different parts can be identified in the coincidence spectrum: (1) a region of high intensity near the green line labeled $E_2 = \Delta E - \phi$ [comparison with the singles spectrum allows one to conclude that this feature corresponds to the excitation of a single plasmon, which is shown separately in Fig. 2(a)]; (2) horizontal stripes along the E_1 scale at energies $E_2 = 3.7$ and 17 eV, indicated by the yellow arrows, which seem to have a counterpart along the E_2 scale (vertical dashed lines marked by yellow arrows; this energy region will be referred to as the plural scattering region in the following); and (3) a strong and structured peak for energies $E_1, E_2 \leq 20$ eV, corresponding to the cascade of secondary electrons. A distinct peak of what appears to be correlated electron emission is seen around the point $(E_1, E_2) = (17, 17)$ eV.

Figure 2(b) shows the region in phase space corresponding to the plasmon loss feature in Fig. 2(a), obtained by applying energy and momentum conservation (see Eqs. 1–3 of [39]) to the data within the red parallelogram in Fig. 2(a). Above the Fermi level, the false colors encode the projected yield of the final state, below the energy and momentum of the bound electron in the initial state. The colored arrows in Fig. 2(b) indicate the interband transitions corresponding to the energies of the fast and slow electrons marked by colored dots in Fig. 2(a).

Finally, in Fig. 3(a), the total electron yield (TEY) measured in absolute units (green curve, [24]) is compared with the coincidence data in Fig. 1 summed over E_1 (blue curve) and the singles SE spectrum (black curve).

A striking feature of the single scattering plasmon feature is the complete absence of the π plasmon in the coincidence data, in particular, also at low energies: finite count rates appear only for $\Delta E > 12$ eV. This can be understood on the basis of the k -space representation of the data in Fig. 2(b): for the characteristic energy loss of the π plasmon and the kinematics of the experiment, no favorable combination of initial and final states above vacuum is available that would allow a transition to take place [24]. Note that our experiment mainly samples a region in phase space where an energy gap between valence and conduction band occurs, far away from the K point.

For any energy loss ΔE in the single scattering plasmon feature the probability for generating a secondary electron has a strong peak at energies E_2 within the plasmon feature. This observation highlights the fact that the final state of the scattering process corresponds to the ejection of a single bound electron. Any conceivable process in which the

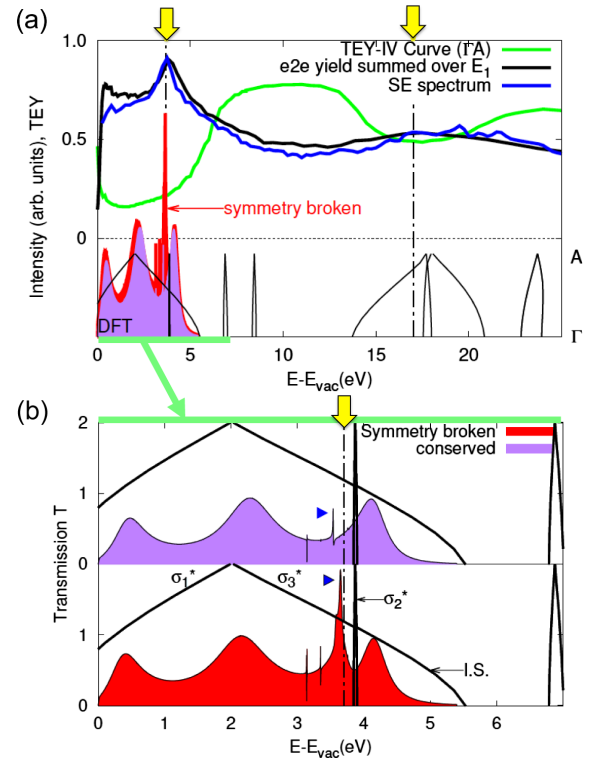


FIG. 3. (a) Green curve: TEY measured in absolute units [24] showing a broad minimum between 0 and 5.5 eV due to the high transmissivity of the interlayer states; blue curve: coincidence data in Fig. 1 summed over E_1 ; black curve: singles SE spectrum (white curve in Fig. 1). The latter two curves exhibit the sharp resonance due to hybridization. The lower panel shows the theoretical total transmission of the graphite surface as a function of initial energy for the symmetry-conserved (purple) and symmetry-broken (red) slab compared with the band structure along ΓA . (b) Expanded view of the lower panel in (a). Blue triangles mark the transmission peak caused by the σ_2^* band. In the symmetry-conserved slab, this resonance is very sharp, containing few electrons, while it becomes much more pronounced in the symmetry-broken slab due to hybridization (see text).

energy is transferred to more than one electron in the final state would lead to intensity below the single scattering plasmon feature for any reasonable energy sharing model. Furthermore, the maximum in the single scattering feature along E_2 is seen to occur for a range of slightly different binding energies (energetic distance from the green diagonal) when going from top to bottom, following the dispersion of the initial state. This is indeed confirmed by the representation of the single scattering data in k space, Fig. 2(b). A faint minimum is seen in the plasmon loss feature in Fig. 1 near $(E_1, E_2) = (154, 10)$ eV, corresponding to the energy gap in between the strongly dispersing interlayer bands along ΓA indicated by the yellow arrows in Fig. 2(b). Indeed, a minimum in the final state intensity is also observed in the plasmon spectrum in Fig. 2(b) at $E - E_F \sim 15$ eV.

These findings show that, for a material with a complex band structure, such as graphite, the excitation of a plasmon and the associated interband transitions are both essential parts of the same coherent process, a plasmon-assisted interband transition [47] leading to ejection of the bound electron into an excited state. This picture supports the momentum-exciton model for the plasmon [24,48] as a coherent excitation of a (rather small) number of electron hole pairs behaving as a quasiparticle with a well-defined energy and momentum. Note that the typical number of electrons participating in a plasmon is about five [48,49] and that the range of possible energies above vacuum occupied by the ejected electron is limited by the plasmon energy. This implies that the width of the secondary electron peak is essentially governed by the density of the solid-state electrons.

The coincidence data also convey the fact that plural inelastic scattering proceeds via a Markov-type process [24,50]; i.e., no memory of the previous collision plays a role in subsequent processes. If this were not the case, i.e., if coherent plural plasmon creation took place in which the full energy loss is transferred to a single electron, intensity due to plasmon replicas should appear just below the green diagonal line at energies $(E_1, E_2) = (E_0 - n \times \hbar\omega_{\pi+\sigma}, n \times \hbar\omega_{\pi+\sigma} - \phi + E_b)$. Here n is an integer and E_b is the (negative) binding energy of the initial state. Likewise, no plasmon replicas are seen for ejected electron energies corresponding to a single plasmon loss, i.e., at energies near $(E_1, E_2) = (E_0 - n \times \hbar\omega_{\pi+\sigma}, \hbar\omega_{\pi+\sigma} - \phi + E_b)$. Instead, stripes of intensity at energies (marked by the yellow arrows) of 3.7 and 17 eV, respectively, are observed. The fact that the ejected electron energy in the plural scattering region is completely independent of ΔE cannot be understood within the simple DL model outlined in the Supplemental Material [39]. The explanation is that, when more than one inelastic process occurs, any combination of scattering angles and energy losses in individual scattering events can lead to the net energy and momentum transfer observed for the ejected electron. In other words, the initial state for the process leading to ejection of the second electron is no longer determined as in the single scattering feature [see Fig. 2(a)]. This implies that the DL model is only valid in the single scattering regime. The final state in the plural scattering regime, however, is determined by the detection geometry and energy of the slow electron. Indeed, the energies at which these stripes appear seem to correspond to the position of the atomlike σ_2^* bands ~ 7.5 eV above Fermi, as well as the flat σ^* bands 22 eV above Fermi, along the ΓA direction [see Fig. 2(b)]. Note that the ΓA direction coincides with the symmetry axis of the TOF analyzer, which measures the final state of the slow electron.

The energies of the secondary electrons emitted along the graphite c axis (stripes in the plural scattering region marked with yellow arrows) and the sharp peak in the SE

spectrum at 3.7 eV exhibiting a surprising lack of dispersion [4,6,7,9–11,24,26,40–42] deserve to be discussed in more detail. These features in the coincidence data appear outside the single scattering region and are attributed to incoherent plural plasmon excitation. As noted above, the initial state is no longer fixed by the experimental kinematics since many combinations of energy and momentum transfers in individual scattering processes yield the same net final state. The final state energies of these features are very close to the flat σ_2^* bands within the interlayer resonances along ΓA [Fig. 2(b)]. To understand the characteristics of these final states, we use DFT calculations [51–55] for bulk graphite, as well as a surface slab to parametrize a tight-binding model [54]. We can then simulate the transmission of the secondary electron from a Bloch state inside the solid (i.e., the final state of the inelastic scattering process with the incoming electron) to a free vacuum state [as given by Eq. (5) in the Supplemental Material [39]]. Given an unperturbed graphite slab, we find, as expected by the flat nature of the σ_2^* bands, a very sharp resonance [see blue triangle in upper panel of Fig. 3(b)] that does not contribute significantly to the overall signal, as its area is vanishingly small. We next aim to model the symmetry breaking induced by the incidence of the primary electron and the emerging plasmon in the simplest way possible: we induce a symmetry breaking at the surface of the slab by a local potential $V_{\delta sp^2} \approx 0.3$ eV added to a single of the three equivalent sp^2 orbitals of each carbon atom of the surface layer. Such a term breaks the D_{6h} symmetry of graphite, essentially locally eliminating the threefold symmetry. The induced hybridization between the σ_2^* bands and $\sigma_{1,3}^*$ interlayer bands substantially enhances and broadens the resonance. The resulting hybrid state exhibits the high density of states of the flat band, implying that it is a favorable state for an initially bound electron to reach a final state above the vacuum level. The hybrid state also has the high mobility of the interlayer state which efficiently couples to vacuum, allowing it to escape from the surface. For simplicity, we neglect a more detailed description of the outgoing electron (e.g., the effect of image charges) by restricting ourselves to outgoing plane waves. Indeed, we have verified numerically that a similar symmetry breaking in bulk HOPG leads to transmission from σ_2^* to $\sigma_{1,3}^*$ modes (and vice versa) in bulk transport perpendicular to the layers.

The above process can be summarized as follows: in response to the incoming particle, electron hole pairs are created in the solid, breaking the symmetry of the system, which can no longer be described by means of a one-electron band structure. In the course of the evolution of the plasmon, an electron is promoted to the state with high density in the unoccupied band structure, leaving a hole in the valence band behind. The group velocity of this state is zero: it is a stationary state corresponding to an oscillation about and between graphene layers. Because of the

plasmon-induced symmetry breaking, this state hybridizes with the interlayer state, with the same phase velocity but with a significant group velocity along the c axis. The nature of the interlayer states can be qualitatively understood by considering the optical analogy to the Fabry-Pérot interferometer [25]. The waves are multiply reflected in between graphene layers, but at the same time the transmissivity is appreciable, leading to transport along the c axis. It is well known that these states couple effectively to vacuum, eventually leading to emission of an electron from the surface. In the above qualitative description, the entire process is conceived to consist of individual steps in time. This was done for conceptual simplicity. More realistically, however, it should be regarded as a single coherent process.

Since the parametrization of our tight-binding model only extends to about 18 eV, the origin of the second stripe in the coincidence data at $E - E_F \sim 17$ eV could not be verified. It is conjectured, however, that a similar hybridization mechanism plays a role in that case as for the lower lying interlayer band around 3.7 eV. The peak of apparent correlated emission at $(E_1, E_2) = (17, 17)$ eV then is a direct consequence of the hybridization in that also the unoccupied flat band at around 17 eV (above vacuum) is a favorable final state, and by virtue of the high mobility of the hybridized state also leads to a strong peak in the secondary electron cascade. For the primary energy $E_0 = 173$ eV employed here, plural inelastic processes can lead to (incoherent) creation of several secondary electrons. A part of these SEs may actually escape and give rise to multielectron detection events with preferred energies of 17 eV. As discussed above, this proceeds via a Markov sequence of events leading to a strong preference of final states with these energies in the course of (incoherent) plural inelastic scattering and generation of secondary electrons. Therefore, while the peak at $(E_1, E_2) = (17, 17)$ eV appears to be due to correlated electron emission, it rather is an incoherent increase in the electron pair intensity due to the aforementioned process. A similar peak is also expected at $(E_1, E_2) = (3.7, 3.7)$ but could not be observed since the lowest energy along the E_1 scale that can be reached in the coincidence experiment is ~ 5 eV.

In summary, the $(\pi + \sigma)$ plasmon in graphite has been resolved with respect to the involved electronic transitions. Formation of a hybrid state as a consequence of plasmon-induced symmetry breaking provides an explanation for the strong resonance observed in SE spectra in the literature (at 3.7 eV in the present Letter). Most importantly, it explains the difference in band structure measurements using elastic processes and techniques that involve creation of a plasmon. To fully appreciate this point, the reader is referred to Fig. 4 in the work by Maeda *et al.* [9], which shows a direct comparison of IPES and SEE data, the dispersion of the interlayer state completely lacking in the latter. The same group later conducted experiments on single layer graphene where the unoccupied states show a nearly free electron

dispersion [56]. This is to be expected since, for a single layer, hybridization with interlayer states cannot occur. Comparison of these results thus highlights a most relevant difference between a true 2D material and a van der Waals material: electron transport and emissivity along the c axis, the subject of the present Letter. The present results therefore indicate that the inverse low energy electron diffraction formalism that is often employed to interpret secondary electron spectra [57] should be complemented to account for many-body processes, since the phenomenon of secondary electron emission cannot be fully described on the basis of the one-electron band structure.

The authors express their gratitude to P. Riccardi and E. Krasovskii for fruitful discussions and P. Riccardi for providing detailed band structure data of graphite. Financial support by the FP7 People: Marie-Curie Actions Initial Training Network (ITN) SIMDALEE2 (Grant No. PITN 606988) is gratefully acknowledged. F.L. and L.L. acknowledge support by FWF program I 3827-N36. The computational results presented have been achieved using the Vienna Scientific Cluster (VSC).

*werner@iap.tuwien.ac.at

†Present address: Laboratorium für Festkörperphysik, ETH Zürich, Auguste-Piccard-Hof 1, Zürich, Switzerland.

‡Present address: ISM-CNR, Via Fosso del Cavaliere 100, 00133 Roma, Italy.

- [1] A. K. Geim and I. V. Grigorieva, *Nature (London)* **499**, 419 (2013).
- [2] K. S. Novoselov and A. H. Castro Neto, *Phys. Scr. T* **146**, 014006 (2012).
- [3] E. A. Taft and H. R. Philip, *Phys. Rev.* **138** (1965).
- [4] R. F. Willis, B. Fitton, and G. S. Painter, *Phys. Rev. B* **9**, 1926 (1974).
- [5] R. Klucker, M. Skibowski, and W. Steinmann, *Phys. Status Solidi (b)* **65**, 703 (1974).
- [6] P. J. Møller and M. H. Mohamed, *J. Phys. C* **15**, 6457 (1982).
- [7] L. Papagno and L. S. Caputi, *Surf. Sci.* **125**, 530 (1983).
- [8] U. Diebold, A. Preisinger, P. Schattschneider, and P. Varga, *Surf. Sci.* **197**, 430 (1987).
- [9] F. Maeda, T. Takahashi, H. Ohsawa, S. Suzuki, and H. Suematsu, *Phys. Rev. B* **37**, 4482 (1988).
- [10] A. Hoffman, G. L. Nyberg, and S. Prawer, *J. Phys. Condens. Matter* **2**, 8099 (1990).
- [11] V. N. Strocov, P. Blaha, H. I. Starnberg, M. Rohlfig, R. Claessen, J.-M. Debever, and J.-M. Themlin, *Phys. Rev. B* **61**, 4994 (2000).
- [12] N. Barrett, E. E. Krasovskii, J. M. Themlin, and V. N. Strocov, *Surf. Sci.* **566–568**, 532 (2004).
- [13] W. S. M. Werner, A. Bellissimo, R. Leber, A. Ashraf, and S. Segui, *Surf. Sci.* **635**, L1 (2015).
- [14] P. Wallace, *Phys. Rev.* **71**, 622 (1947).
- [15] J. C. Slonczewski and P. R. Weiss, *Phys. Rev.* **109**, 272 (1958).
- [16] G. S. Painter and D. E. Ellis, *Phys. Rev. B* **1**, 4747 (1970).

- [17] N. A. W. Holzwarth, S. G. Louie, and S. Rabii, *Phys. Rev. B* **26**, 5382 (1982).
- [18] R. C. Tatar and S. Rabii, *Phys. Rev. B* **25**, 4126 (1982).
- [19] A. G. Marinopoulos, L. Reining, V. Olevano, A. Rubio, T. Pichler, X. Liu, M. Knupfer, and J. Fink, *Phys. Rev. Lett.* **89**, 076402 (2002).
- [20] T. Fauster, F. J. Himpsel, J. E. Fischer, and E. W. Plummer, *Phys. Rev. Lett.* **51**, 430 (1983).
- [21] H. Hibino, H. Kageshima, F. Maeda, M. Nagase, Y. Kobayashi, and H. Yamaguchi, *Phys. Rev. B* **77**, 075413 (2008).
- [22] R. M. Feenstra, N. Srivastava, Q. Gao, M. Widom, B. Diaconescu, T. Ohta, G. L. Kellogg, J. T. Robinson, and I. V. Vlassiuk, *Phys. Rev. B* **87**, 041406(R) (2013).
- [23] J. Jobst, J. Kautz, D. Geelen, R. M. Tromp, and S. J. Van Der Molen, *Nat. Commun.* **6**, 8926 (2015).
- [24] A. Bellissimo, G.-M. Pierantozzi, A. Ruocco, G. Stefani, O. Ridzel, V. Astašauskas, M. Taborelli, and W. S. M. Werner, *J. Electron Spectrosc. Relat. Phenom.* **241**, 146883 (2019).
- [25] D. Geelen, J. Jobst, E. E. Krasovskii, S. J. van der Molen, and R. M. Tromp, *Phys. Rev. Lett.* **123**, 086802 (2019).
- [26] A. Hoffman, G. L. Nyberg, and S. Prawer, *J. Phys. Condens. Matter* **2**, 8099 (1990).
- [27] T. Eberlein, U. Bangert, R. R. Nair, R. Jones, M. Gass, A. L. Bleloch, K. S. Novoselov, A. Geim, and P. R. Briddon, *Phys. Rev. B* **77**, 233406 (2008).
- [28] Kenneth W.-K. Shung, *Phys. Rev. B* **34**, 979 (1986).
- [29] M. F. Lin, C. S. Huang, and D. S. Chuu, *Phys. Rev. B* **55**, 13961 (1997).
- [30] N. Papageorgiou, M. Portail, and J. M. Layet, *Surf. Sci.* **454**, 462 (2000).
- [31] L. Calliari, S. Fanchenko, and M. Filippi, *Surf. Interface Anal.* **40**, 814 (2008).
- [32] L. Calliari, S. Fanchenko, and M. Filippi, *Carbon* **45**, 1410 (2007).
- [33] M. Guzzo, J. J. Kas, L. Sponza, C. Giorgetti, F. Sottile, D. Pierucci, M. G. Silly, F. Sirotti, J. J. Rehr, and L. Reining, *Phys. Rev. B* **89**, 085425 (2014).
- [34] D. Voreades, *Surf. Sci.* **60**, 325 (1976).
- [35] M. R. Scheinfein, J. Drucker, J. Liu, and J. K. Weiss, *Phys. Rev. B* **47**, 4068 (1993).
- [36] H. Mülleijans, A. L. Bleloch, A. Howie, and M. Tomita, *Ultramicroscopy* **52**, 360 (1993).
- [37] F. J. Pijper and P. Kruij, *Phys. Rev.* **44**, 9192 (1991).
- [38] W. S. M. Werner, F. Salvat-Pujol, A. Bellissimo, R. Khalid, W. Smekal, M. Novak, A. Ruocco, and G. Stefani, *Phys. Rev. B* **88**, 201407(R) (2013).
- [39] See Supplemental Material at <http://link.aps.org/supplemental/10.1103/PhysRevLett.125.196603> for a concise description of the experimental procedure, as well as the physical model and the theoretical approach employed to analyse the experimental data and interpret the results.
- [40] A. R. Law, M. T. Johnson, and H. P. Hughes, *Phys. Rev. B* **34**, 4289 (1986).
- [41] L. S. Caputi, G. Chiarello, A. Santaniello, E. Colavita, and L. Papagno, *Phys. Rev. B* **34**, 6080 (1986).
- [42] I. Schäfer, M. Schlüter, and M. Skibowski, *Phys. Rev. B* **35**, 7663 (1987).
- [43] P. Riccardi (private communication).
- [44] A. Ruocco, M. Milani, S. Nannarone, and G. Stefani, *Phys. Rev. B* **59**, 13359 (1999).
- [45] A. Liscio, A. Ruocco, G. Stefani, and S. Iacobucci, *Phys. Rev. B* **77**, 085116 (2008).
- [46] A. S. Kheifets, S. Iacobucci, A. Ruocco, R. Camilloni, and G. Stefani, *Phys. Rev. B* **57**, 7360 (1998).
- [47] K. A. Kouzakov and J. Berakdar, *Phys. Rev. A* **85**, 022901 (2012).
- [48] R. A. Ferrell and J. J. Quinn, *Phys. Rev.* **108**, 570 (1957).
- [49] I. Egri, *Z. Phys. B* **53**, 183 (1983).
- [50] W. S. M. Werner, F. Salvat-Pujol, W. Smekal, R. Khalid, F. Aumayr, H. Störi, A. Ruocco, F. Offi, G. Stefani, and S. Iacobucci, *Appl. Phys. Lett.* **99**, 184102 (2011).
- [51] G. Kresse and J. Furthmüller, *Comput. Mater. Sci.* **6**, 15 (1996).
- [52] N. Marzari and D. Vanderbilt, *Phys. Rev. B* **56**, 12847 (1997).
- [53] I. Souza, N. Marzari, and D. Vanderbilt, *Phys. Rev. B* **65**, 035109 (2001).
- [54] L. Linhart, M. Paur, V. Smejkal, J. Burgdörfer, T. Mueller, and F. Libisch, *Phys. Rev. Lett.* **123**, 146401 (2019).
- [55] F. Libisch, S. Rotter, and J. Burgdörfer, *New J. Phys.* **14**, 123006 (2012).
- [56] H. Hibino, H. Kageshima, F.-Z. Guo, F. Maeda, M. Kotsugi, and Y. Watanabe, *Appl. Surf. Sci.* **254**, 7596 (2008).
- [57] H. Lüth, *Solid Surfaces, Interfaces and Thin Films*, 6th ed. (Springer, Berlin-Heidelberg-New York, 2010).